DOI:10. 13471/j. cnki. acta. snus. 2021D012

Effects of coastline and terrain on warm-sector heavy rainfall in the Pearl River Delta, South China*

CHEN Zijian[1,2], *LIN Wenshi*[1,2], *JIANG Baolin*[3], *CAO Qimin*[1], *SHEN Xiaodian*[1]

1. *Southern Marine Science and Engineering Guangdong Laboratory(Zhuhai), Zhuhai 519082, China*
2. *School of Atmospheric Sciences / Guangdong Province Key Laboratory for Climate Change and Natural Disaster Studies, Sun Yat-sen University, Zhuhai 519082, China*
3. *School of Geography and Tourism, Huizhou University, Huizhou 516007, China*

Abstract: We conducted three experiments using the WRF-Chem model to examine the physical effects of the coastline and numerous low mountains along the coast in the Pearl River Delta (PRD) area on the intensity and distribution of warm-sector heavy rainfall. We analyzed dynamic effects and water vapor transport, and found that by replacing the mountains in the PRD with flat land, orographic lifting disappears, resulting in a considerable reduction of coastal convergence and water vapor accumulation at 925 hPa along the coastline; the 12 hours accumulated precipitation area is mainly confined to the north of 22. 7°N which is 80 km north than without moving out the mountains, and precipitation intensity decreases. By shifting the coastline northward and thus, removing the special topography of the low mountains and the contrast of frictional forces along the original coastline, the convection caused by the convergence is greatly reduced. As a result, almost no precipitation falls in the PRD region. Instead, convection, water vapor accumulation and precipitation centers appear near the new coastline because of orographic lifting and discontinuities in surface friction. The coastline and coastal mountains of the PRD play important roles in the occurrence, intensity and distribution of precipitation.

Key words: warm-sector heavy rainfall; coastline; terrain; WRF-Chem model; the Pearl River Delta area
CLC number: P445　**Document code**: A　**Article number**: 2097 - 0137（2022）01 -0062 -14

华南珠三角地区海岸线和地形对暖区暴雨的影响

陈子健[1,2]，林文实[1,2]，蒋宝林[3]，曹琪敏[1]，沈晓钿[1]

1. 南方海洋科学与工程广东省实验室(珠海),广东 珠海 519082
2. 中山大学大气科学学院/广东省气候变化与自然灾害研究重点实验室,广东 珠海 519082
3. 惠州学院地理与旅游学院,广东 惠州 516007

摘　要：通过使用WRF-Chem模式进行3个敏感性试验，研究东亚夏季风背景下，华南珠三角地区复杂的海岸线和沿岸众多低矮的山脉地形与暖区暴雨强度和分布之间的物理关联。通过动力以及水汽输送分析，发现当珠三角地区的低矮山脉地形移除后，山脉群对气流的地形抬升以及辐合作用消失，海岸线上的对流活动明显减少，925 hPa上水汽在海岸线上的积累减少，降雨区域向北移动约80 km，降水强度也减弱；当沿岸山脉地形移除，海岸线北移，喇叭口特殊地形消失后，原来海岸线上的海陆摩擦力差异消失，气流的辐合对流运动大幅减少，

* **收稿日期**：2021 - 02 - 26　**录用日期**：2021 - 03 - 11　**网络首发日期**：2021 - 07 - 16
基金项目：国家重点研发计划项目(2018YFC1507402)；国家自然科学基金(41875168)；广东省气候变化与自然灾害研究重点实验室基金(2020B1212060025)
作者简介：陈子健(1995 年生), 男; **研究方向**: 中小尺度天气; E-mail: chenzj59@mail2. sysu. edu. cn
通信作者: 林文实(1965 年生), 男; **研究方向**: 中小尺度天气动力学、数值天气预报; E-mail:linwenshi@mail. sysu. edu. cn

珠三角区域内几乎没有降水，取而代之的是在新的海岸线沿岸附近由于地形抬升作用以及下垫面摩檫力的差异，出现新的对流活动以及水汽的堆积，并且新海岸线上出现新的降水中心。因此珠三角区域内海岸线以及海岸山地是影响降水强度、分布和发生发展的重要因素。

关键词： 暖区暴雨；海岸线；地形；WRF-Chem模式；珠三角地区

1 Introduction

In South China, under the influence of the East Asian summer monsoon, the first rainy season of each year begins in April and ends in June, and has unique regional characteristics. Precipitation can be in the form of frontal precipitation caused by the frontal system as a result of the southward movement of the mid-latitude westerlies. It can also be in the form of warm-sector heavy rainfall[1-2]. Warm-sector heavy rainfall generally refers to precipitation that occurs in the warm area on the southern side of the surface frontal system, or in the warm zone at 200−300 km(or even greater distances) from the southern side of the frontal system. It could sometimes occur at the confluence of the southwesterly and southeasterly flows, or even in the non-shear cold southwesterly flow between Nanling Mountains in Guangdong Province and the northern part of the South China Sea where fronts are absent [1]. The warm-sector heavy rainfall in South China that appears during the first rainy season of the year generally occurs in the warm zone at 200−300 km from the southern side of the frontal system. Compared with frontal precipitation, warm-sector heavy rainfall is higher in intensity, longer in duration and occurs over a smaller area. When warm-sector heavy rainfall occurs in South China, southerly winds prevail at the middle and low altitudes, and there is no forcing from distinct weather-scale baroclinic systems. As a result, it is difficult to predict warm-sector heavy rainfall before it occurs or to explain the cause of it systematically afterwards [3-4]. Therefore, warm-sector heavy rainfall can lead to floods extremely easily, threatening social and economic development as well as personal and property safety.

Moist and deep convections occur frequently in the Asian summer monsoon region, resulting in large amounts of precipitation, especially in coastal areas [5-7], such as along the South China coast [8]. Convective systems are active along the South China coast and can cause extreme weather (such as thunderstorms, strong winds, heavy rainfall and floods) in densely populated coastal areas [9]. The ocean, coastline and coastal mountains are the three most important physical factors that affect the occurrence and development of convection during the monsoon period in South China [9-10]. The ocean mainly provides warm and humid air flows [11]. The coastline causes discontinuities in surface friction and temperature, which facilitate convergence of the lower layers and expands the area of precipitation over the coast [12-14]. Mountains play a role in orographic lifting and promote the convergence and occurrence of convective activities [15-16]. In addition, when the low-level jet that is humid and strong impinges the mountains, a large amount of water vapor is accumulated near the windward slope because of orographic lifting [17-19]. The obstruction of low-level jets by mountains of different shapes(including height and width) affects the intensity and distribution of coastal precipitation[20-23].

In East Asia, precipitation occurs frequently along coastlines causing huge economic losses. Numerous studies on the influence of mountains on precipitation have focused on southwestern Taiwan[24-28]. Under the influence of the East Asian monsoon, heavy precipitation occurs along the southwestern coast of Taiwan as the southwesterly jet in the lower troposphere flows through the Central Mountain Range and is lifted[19]. Davis and Lee[25] conducted an experiment to study the influence of topography on precipitation during the Southwest Monsoon near Taiwan. Over the relatively flat terrain of South Korea, a convergence zone forms as a result of the discontinuity between sea and land roughness, and leads to continuous heavy precipitation over the western coast[13]. The diverse mountainous terrain and coastline of China also have various effects on precipitation. Nocturnal low-level jets are lifted on the windward slope over the complex terrain of eastern China. This leads to local convergence, which likely triggers the formation of mesoscale convective systems [29-31].

Coastal convergence and orographic lifting strongly impact the triggering and development of convection and precipitation near the South China coast [9, 32-37]. Focusing on southern China, its large-scale topography and the small-scale coastal mountains near Lufeng, Du et al. [10] studied the influence of coastal topography and coastline on convection initiation and upscale convective growth.

The Pearl River Delta(PRD) in southern China is densely populated and has a high level of economic development. Few studies have examined the impact of the complex PRD coastline and the numerous small and low mountains along the coast on warm-sector heavy rainfall. Therefore, in this study we examine the relationships and feedback mechanisms between topography of the PRD and warm-sector heavy rainfall under the influence of the East Asia Summer monsoon, focusing on the complex coastline and low mountains of the PRD and warm-sector heavy rainfall distribution and intensity.

2 Data,model description and experimental design

For observation data of accumulated precipitation in the study area, we used a merged precipitation product developed by National Meteorological Information Center of the China Meteorological Administration. It has a horizontal resolution of 0. 1° and temporal resolution of 1 h, and is based on data from land-based automatic weather stations in China and precipitation estimates derived from satellite data using the Climate Prediction Center morphing method (CMORPH) [38].

As chemistry and meteorology are fully coupled in the Weather Research and Forecasting model coupled with Chemistry(WRF-Chem), it is a more authentic representation to study the process of rainfall in PRD where the pollutant of aerosols is serious. And hence, the WRF-Chem model(version 4. 2. 1) with three nested domains was used in this study. Fig. 1 shows the model domains. The outermost domain (D01) with a horizontal grid resolution of 36 km contains nested domains D02 and D03 with horizontal grid resolutions of 12 and 4 km, respectively. All experiments were run from 1200 UTC 10 May 2014 to 0000 UTC 12 May 2014 and initialized with the National Centers for Environmental Prediction Final (NCEP-FNL) global tropospheric analysis dataset (http://rda. ucar. edu/datasets/ds083. 2). Initial and lateral boundary conditions were updated every 6 h. Observations from weather stations were assimilated into the model initial conditions [39]. The first 12 h of simulation time was regarded as the spin-up time. To improve simulation results in the boundary layer, 40

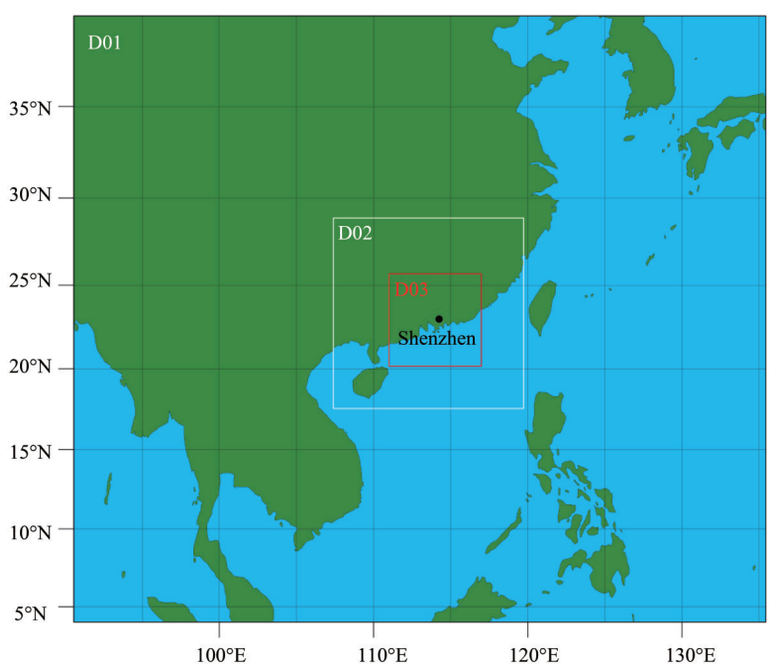

Fig. 1 WRF-Chem model domain with three nested domains: D01, D02 (white boxes) and D03 (red box)

vertical levels were used(η levels: 1.000, 0.995, 0.993, 0.990, 0.983, 0.978, 0.970, 0.962, 0.954, 0.944, 0.934, 0.909, 0.880, 0.845, 0.807, 0.765, 0.719, 0.672, 0.622, 0.571, 0.520, 0.468, 0.420, 0.376, 0.335, 0.298, 0.263, 0.231, 0.202, 0.175, 0.150, 0.127, 0.106, 0.088, 0.070, 0.055, 0.040, 0.026, 0.013, 0.000) with the top level at 50 hPa.

The Grell-3 cumulus parameterization scheme[40] was used in domains D01 and D02. However, no parameterization scheme of cumulus convection was adopted in domain D03 because the high resolution of the domain allows quantities at the cumulus scale to be resolved. All domains used the microphysics scheme of Lin et al[41] and the Yonsei University(YSU) boundary layer scheme [42]. The Rapid Radiative Transfer Model for Global Climate Models(RRTMG) longwave and shortwave radiation schemes [43] were adopted for radiation physics. The unified Noah land surface model [44] and the revised MM5 Monin-Obukhov surface-layer scheme were also used [45].

In WRF-Chem, the Carbon-Bond Mechanism version Z(CBM-Z) [46] was adopted for gas-phase atmospheric chemistry. The Model for Simulating Aerosol Interactions and Chemistry(MOSAIC) [47] using eight sectional aerosol bins was used for the aerosol module. The Fast-J scheme [48-49] was used for photolytic reaction rates. For anthropogenic emissions, we used data from the Multi-resolution Emission Inventory for China(MEIC) data (http://www. meicmodel. org) [50]. For biogenic emissions, we used output from the Model of Emissions of Gas and Aerosols from Nature(MEGAN)[51].

To study the influence of the coastline and coastal topography of the PRD on the intensity and location of warm-sector heavy rainfall in South China, one control and two sensitivity experiments were conducted in WRF-Chem. Model output was analyzed to examine the relationships between warm-sector heavy rainfall and changes in the coastline and topography in terms of water vapor transport and other dynamic mechanisms.

Fig.2 shows terrain height settings for the control run(CTL; Fig.2a) and the sensitivity(HGT0 and SEA) experiments. In the sensitivity experiment HGT0 (Fig.2b), the effect of orography was removed by setting the height of the PRD region(21. 5°−24°N, 112°−115. 5°E; indicated by red boxes in Figs.2b and c) to 0 m above sea level. In the sensitivity experiment SEA(Fig. 2c), the land-use type of the PRD region was set to ocean, with a new coastline in the northern part of the region.

3　Case overview and results from the control experiment

To clarify the influence of the coastline and the distribution of the low mountain ranges of the PRD on the warm-sector heavy rainfall in South China, we studied a typical heavy rainfall event that occurred on 11−12 May 2014 UTC. During this event, the main

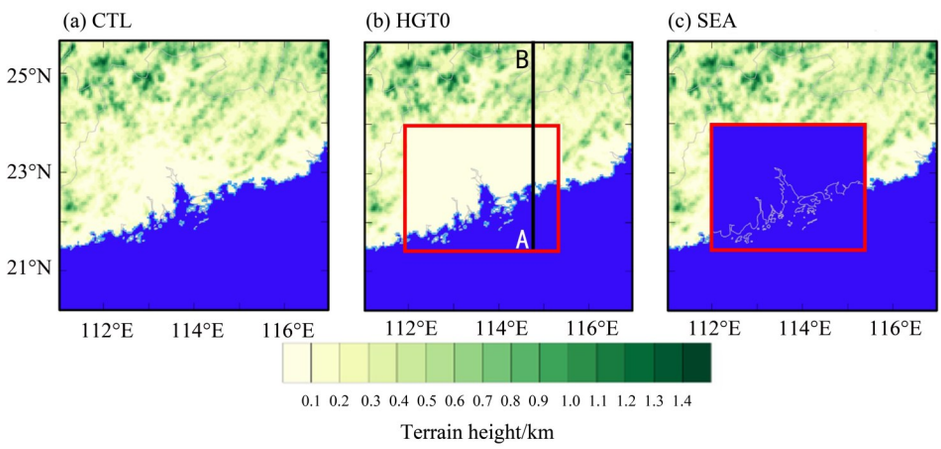

Blue indicates land-use type is set as ocean. In (b) and (c), red boxes indicate the PRD region. In (b), the terrain height in the red box is 0 km, and the black line between A and B indicates location of cross-sections shown in Figs. 9 and 10.

Fig. 2　Terrain height (shading) in D03 for experiments CTL, HGT0, and SEA

precipitation occurred over the PRD, with the precipitation center roughly located on the South China coast near Shenzhen, Guangdong Province(the black dot in Fig. 1). The event occurred between 0000 UTC 11 May and 0000 UTC 12 May 2014. At Shenzhen city, the 6-h averaged precipitation from 0000 to 0600 UTC 11 May 2014 reached 226 mm, and maximum precipitation reached 276. 5 mm. Heavy rains throughout the city and extremely heavy rains in some areas severely damaged and threatened personal safety and property. Therefore, we chose 0000 UTC 11 May to 0000 UTC 12 May 2014 as our study period.

Fig. 3 shows observation data and simulation results from the control run for the 6-h accumulated precipitation from 0000 to 0600 UTC 11 May 2014, the 12-h accumulated precipitation from 0000 to 1200 UTC 11 May 2014, and the 24-h accumulated precipitation from 0000 UTC 11 to 0000 UTC 12 May 2014 for our study area of 21. 5° −24° N, 112° −115. 5° E, which includes the PRD and some offshore areas along the coast. Two main precipitation processes were active. There was a frontal rainband at approximately 25° N and precipitation along the coastline of the PRD(red box in Fig. 3). We focused on the latter, which was a typical warm-sector heavy rainfall process. In terms of the 6-h accumulated precipitation (Figs. 3a, d) from 0000 to 0600 UTC 11 May 2014, simulation results are relatively scattered spatially, but the average intensity and location of simulated precipitation are consistent with those of observation data. Fig. 4 shows that the trend and intensity of the hourly evolution of simulated average precipitation in the PRD are relatively consistent with those of observation data. Fig. 3b, c, e and f show that the average intensity and distribution of simulated 12-h (0000-1200 UTC 11 May 2014) and 24-h (0000 UTC 11 May-0000 UTC 12 May 2014) rainfall are also consistent with those of observation data. However, simulated precipitation is relatively scattered spatially, and

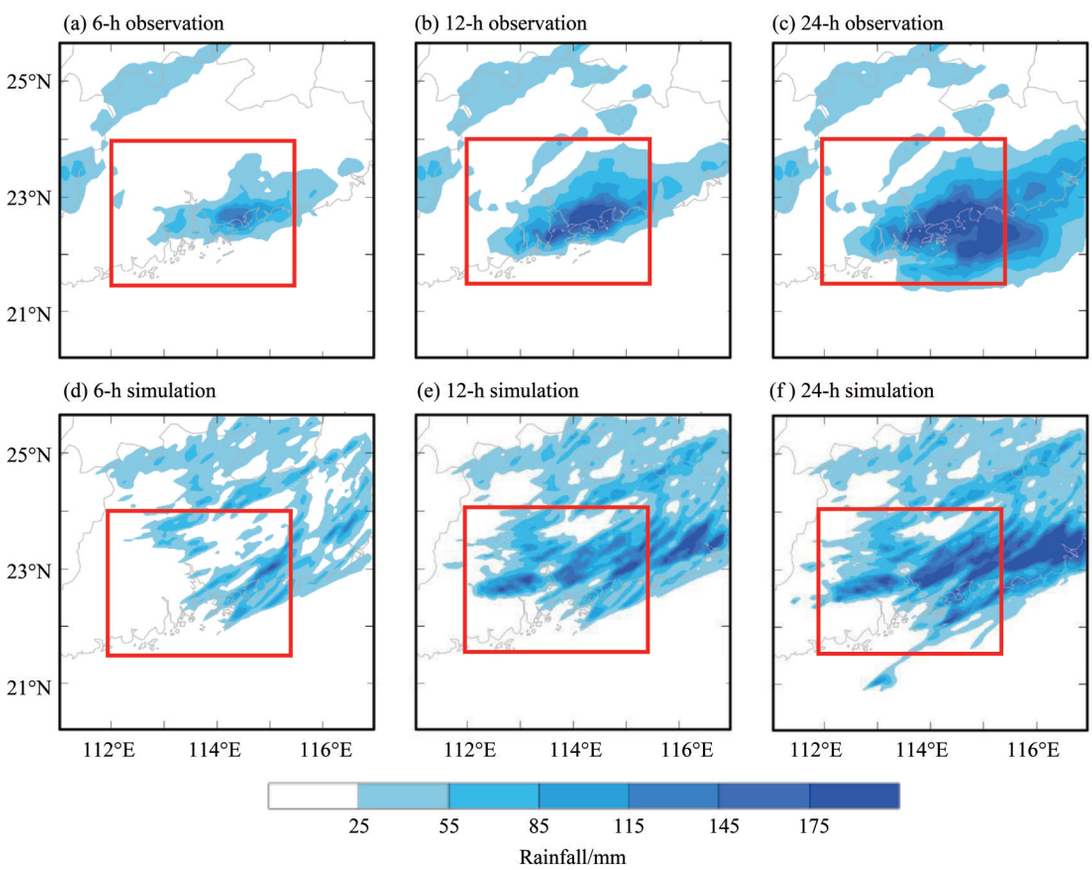

In (a)-(f), red boxes indicate the study area, the Pearl River Delta region.

Fig. 3 The 6-h, 12-h, and 24-h accumulated precipitation (shading) in domain D03 (see Fig. 1) from (a)-(c) observation data and (d)-(f) simulation results from CTL

the precipitation center that is prominent in the observation data is absent in simulation results. Fig. 4 shows that the average precipitation between 0000 UTC 11 May and 0000 UTC 12 May in CTL is below that in observation data. This is because the simulated precipitation area has shifted eastward and out of the PRD during this period.

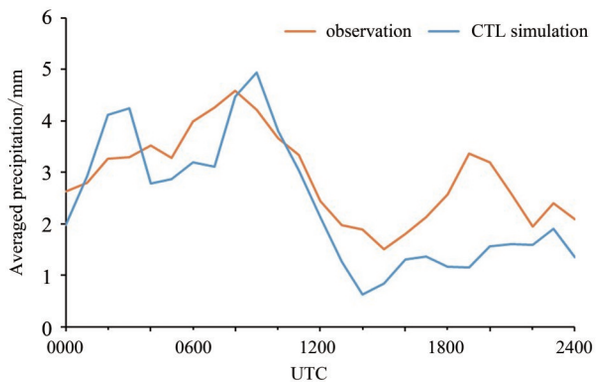

Fig. 4　Hourly evolution of averaged precipitation in the PRD from observation data and CTL simulation between 0000 UTC 11 May 2014 and 0000 UTC 12 May 2014

4　Results and Discussion

4. 1　Topographic effect

To identify the impact of the special coastal and mountain topography of the PRD and the land-sea contrast on the simulation of precipitation, we examined precipitation intensity and distribution from the control run CTL (Figs. 5a, d and g) and the sensitivity experiments HGT0 (Figs. 5b, e and h) and SEA (Figs. 5c, f and i). In HGT0 (Fig. 5b), the low mountains of the PRD (red box in Fig. 5b) are absent leading to the absence of orographic lifting and subsequent vertical convection. Therefore, the 6-h accumulated precipitation from 0000 to 0600 UTC 11 May 2014 shows no obvious precipitation in the PRD, and only scattered precipitation falls along the coastline and the northern boundary of the PRD. In SEA (Fig. 5c), the coastline is shifted northward. Therefore, the 6-h accumulated precipitation shows almost no rainfall in the PRD. For the first 6-h of the simulation period, area with high precipitation rates in the PRD from each of the two sensitivity experiments is only approximately one-sixth of that in CTL (Fig.6).

In HGT0 (Fig. 5e), precipitation occurs in the northern part of the PRD between 0000 and 1200 UTC 11 May, its distribution region is mainly confined to the north of 22. 7° N which is 80 km north than in CTL (yellow line in Fig. 5d and e), and area with high precipitation rates (Fig. 6) is comparable to that in CTL (Fig. 5e), but rainfall intensity is lower in the absence of topography. In SEA (Fig. 5f), almost no precipitation occurs in the PRD because of the northward shift of the coastline and the absence of mountains. There is a small area of precipitation and a new precipitation center near the new coastline in the northern part of the PRD. However, precipitation intensity is relatively low and area with heavy precipitation is close to zero at 0000 - 0800 UTC 11 May. Area with high precipitation rate (Fig. 6) increases after 0900 UTC. Fig. 5f shows that heavy precipitation is mainly concentrated near the new coast.

In terms of 24-h accumulated precipitation (Figs. 5g-i) from 0000 UTC 11 to 0000 UTC 12 May 2014, HGT0 shows two precipitation centers with most precipitation concentrated over the northern part of the PRD(Fig. 5h); SEA shows no precipitation in the center of the PRD, but noticeable precipitation with a center over the new coastline(Fig. 5i). Area with hourly precipitation exceeding 20 mm in SEA increases sharply after 1200 UTC 11 May, and is nearly double that in CTL(Fig.6). These results show precipitation shifting with the coastline; precipitation is delayed and weakened when the coastline is shifted northward and land in the PRD is replaced by ocean. These results indicate the important role that the coastline plays in triggering and sustaining the precipitation process.

The absence of mountains close to the coast in HGT0 therefore results in precipitation that occurs mainly in the northern part of the PRD that is less intense, later and over a smaller area than in CTL. With flat terrain, the surface friction coefficient is reduced and there is no orographic lifting of the low-level jet. The important conditions for triggering convection are missing leading to the absence of the vertical convection system and the reduced area of precipitation. When the land in the PRD is replaced by ocean, a new coastline is created around the PRD area. Precipitation in the PRD disappears. A precipitation center appears over the new coastline along the upper edge

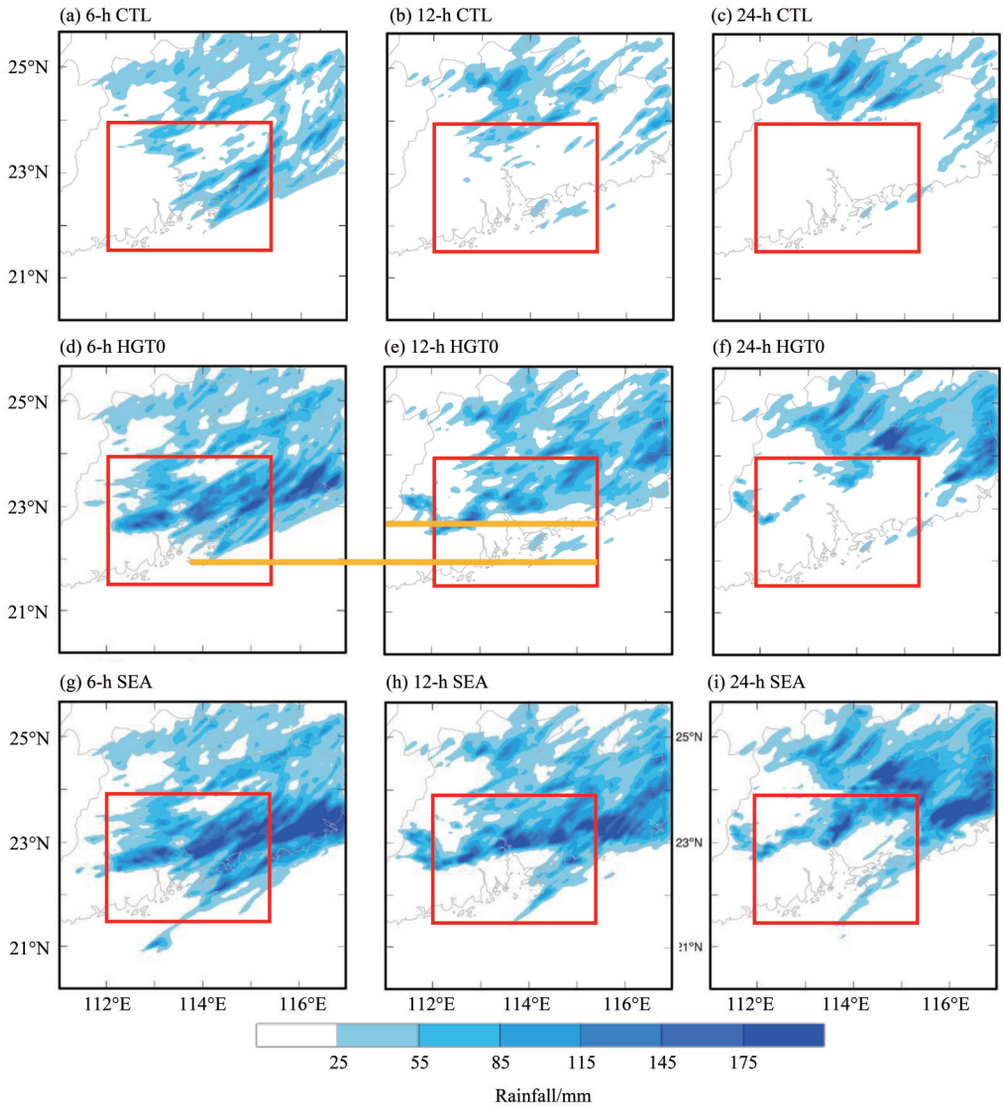

In (a)-(i), red boxes indicate the study area (PRD), yellow lines are used to mark the precipitation range.

Fig. 5 The 6-h, 12-h, and 24-h accumulated precipitation (shading) in domain D03 from simulation results from (a), (d) and (g) CTL, (b), (e) and (h) HGT0, and (c), (f), and (i) SEA at (a)-(c) 0000−0600 UTC 11 May, (d)-(f) 0000−1200 UTC 11 May, and (g)-(i) 0000 UTC 11 May−0000 UTC 12 May 2014

of the red box in Fig. 5i. New rainbands also appear because of the new coastline and the mountains near it. Topography and coastlines can affect or determine the triggering and development of convection[10]. Hence, the sensitivity experiments show that the coastline and the mountains of the PRD play important roles in the occurrence, intensity and distribution of precipitation.

4. 2 Dynamic effects

In this section, we conduct an in-depth examination of the dynamic mechanisms between warm-sector heavy rainfall in the PRD and the influence of the coastline and low mountain ranges. Figures 7 and 8 show the fields of vertical velocity, divergence and horizontal wind at 975 hPa. Vertical profiles of wind velocity and vertical velocity are shown in Figs. 9 and 10. Fig. 7a indicates the presence of a wide mountain range consisting of low mountains in the PRD, which causes vertical flow when the southeasterly and southerly flows in CTL impinge the coastline and mountains. Because of orographic lifting, updraft is formed on the windward slope of the mountains and downdraft appears on the leeward slope. Convergent upward movement near the coastline and windward slope is even more visible in Fig. 8a. The vertical profiles in Figs. 9a and 10a show considerable lifting of

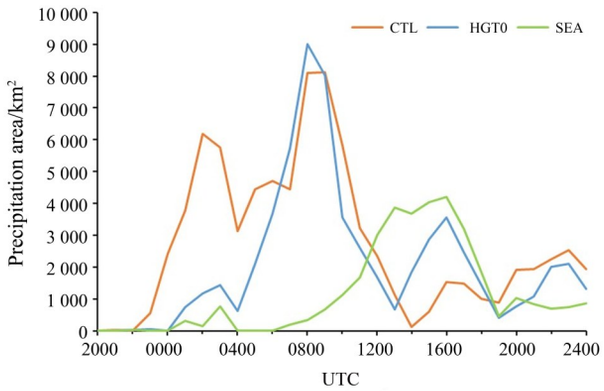

Fig. 6　Hourly evolution of area in the PRD with high precipitation rates (> 20 mm/h) (enclosed by the red box in Fig.5) from the CTL run (orange line), the HGT0 experiment (blue line) and the SEA experiment (green line) between 2000 UTC 10 May and 0000 UTC 12 May 2014

the flow above the coast and mountains. Fig. 10a shows considerable increase in ascending vertical velocity, especially at 23° N, and considerable increase in descending vertical velocity on the leeward slope. Therefore, many convective cells appear in the PRD, which is one of the important factors underlying the formation of warm-sector heavy rainfall in South China.

In HGT0, vertical movement at 975 hPa is mainly concentrated on the windward slope of the mountains in the northern part of the PRD(Fig. 7b). Convergent upward movements(Fig. 8b) occur near the coastline even when terrain height in the PRD is set to 0 m. Wind speeds of low-level jets are clearly lower along the coastline(black dashed line in Fig.9b) than at sea. This is because the flow experiences greater friction over land than over the ocean, resulting in convergence at lower levels and dynamic lifting. This is clearly shown in the vertical profile in Fig.10b. Vertical velocity increases at 900 and 750 hPa along the coastline(black dashed line in Fig.10b), indicating vertical ascending movement caused by convergence. In SEA, the vertical wind field at 975 hPa is mainly concentrated along the new coastline, which is in the northern part of the PRD(Fig. 7c); because land in the PRD is replaced by ocean, friction on the flow is uniform. Unlike HGT0, there is no decrease in velocity or clear convergence along the coastline(Fig. 8b), and convergence mainly occurs along the new coastline

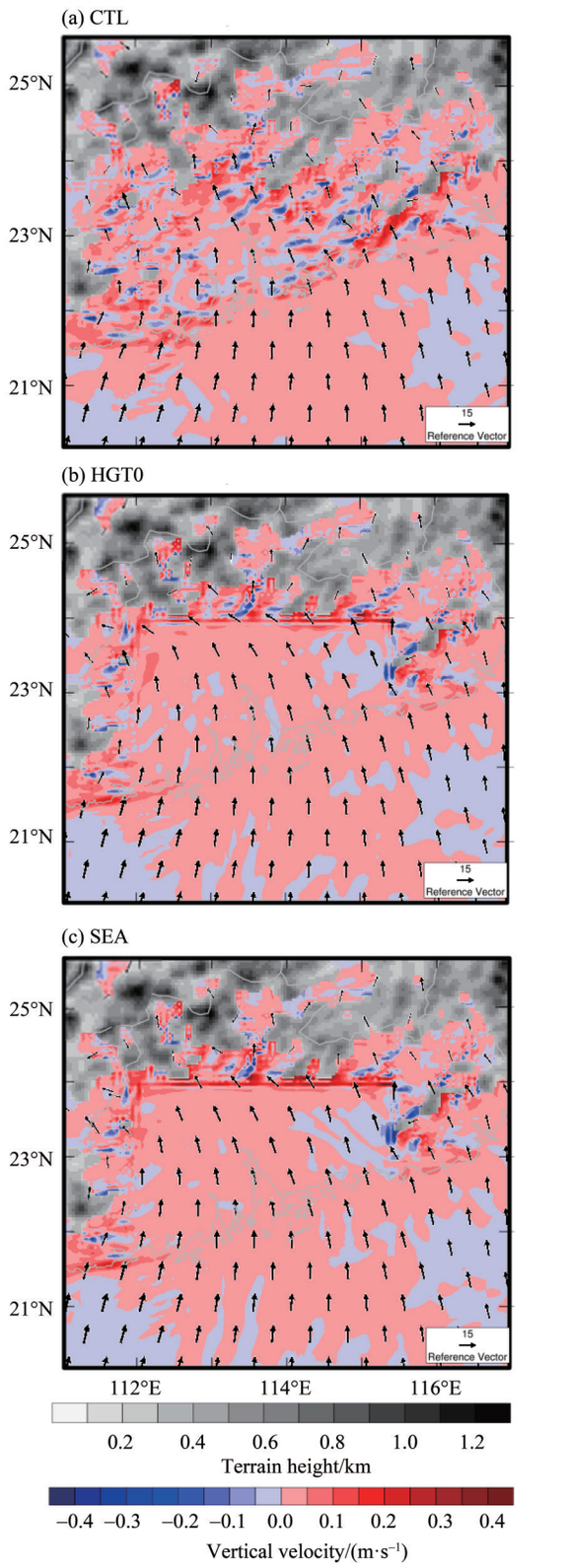

Fig. 7　Terrain height (gray-scale shading) overlaid with vertical velocity (color shading) and horizontal wind velocity at 975 hPa (vectors) in domain D03 (see Fig.1) for CTL, HGT0 and SEA runs at 2000 UTC 10 May, 2014

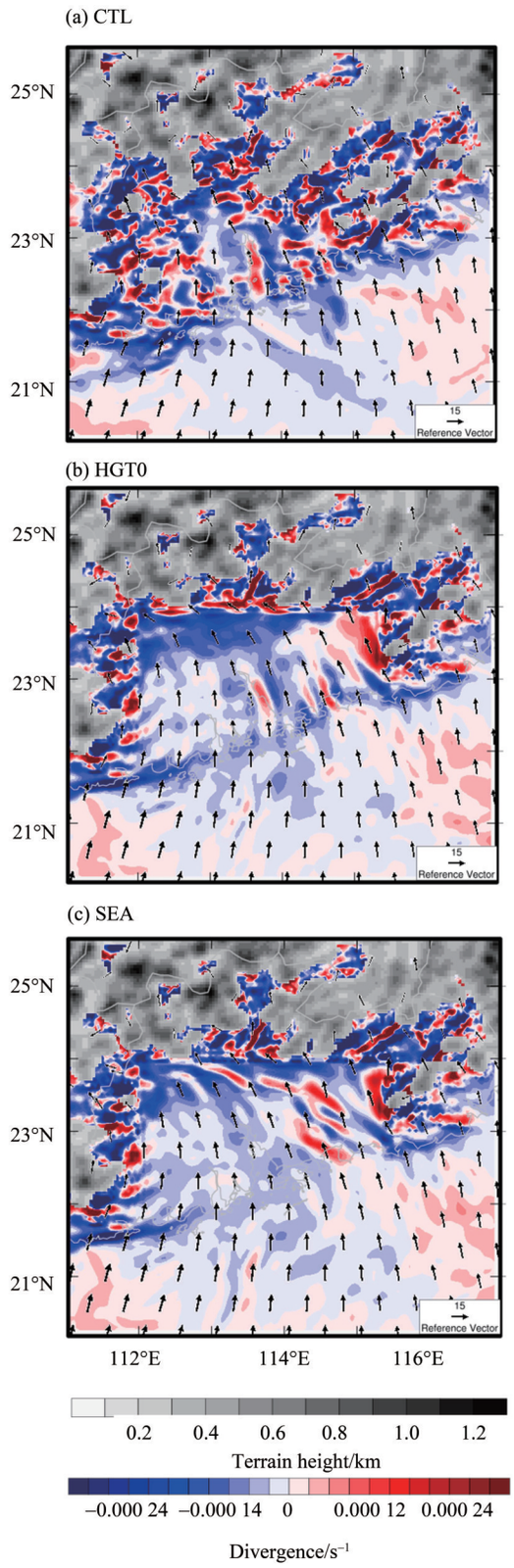

Fig. 8 Terrain height (gray-scale shading) overlaid with divergence (color shading) and horizontal wind velocity at 975 hPa (vectors) in domain D03 (see Fig.1) for the CTL, HGT0 and SEA runs at 2000 UTC 10 May 2014

(Fig. 8c). Convergent upward movement mainly occurs in the northern part of the PRD because of the new coastline and mountains (Figs.9 b and c). Velocities of vertical upward movements along the new coastline(black dashed line in Figs. 9c and 10c) exceed 0. 4 m/s between 1 000 and 800 hPa.

The sensitivity experiments show that the frictional forces exerted by the coastline on air flow and orographic lifting by the mountains are the key factors underlying convergence, which lead to convection initiation and upscale convective growth. Bai et al. [9] proposed that convection initiation may also occur after midnight as a result of the convergence of onshore monsoon flows and land breeze or downslope winds.

In this section, we present our in-depth analysis of the impact of the coastline and small-scale topography on the precipitation process in the PRD. In section 4. 3, we will present our analysis of the influence of topography and coastline on precipitation in terms of water vapor transport.

4. 3 Thermodynamic effects

Water vapor is indispensable for precipitation. In this section, we conduct an in-depth study of the impact of the interaction between water vapor and the coastline and topography of the PRD on the warm-sector heavy rainfall of South China. Fig. 11 shows the horizontal distribution of the water vapor mixing ratio at 925 hPa. In CTL(Fig. 11a), the flow of moist air is blocked by mountain and coastline topography. Thus, large amounts of moisture are locked in the PRD, and the water vapor mixing ratio exceeds 18. 4 and 17. 2 g/kg in the coastal area and over the entire region, respectively(Fig. 11a). In HGT0(Fig. 11b), there are no mountains to block the flow. Therefore, moisture from the ocean does not concentrate in the coastal area. At only approximately 16−17 g/kg, the water vapor mixing ratio in the PRD is relatively low. Unlike CTL, there is no zone of water vapor convergence with high water vapor mixing ratio in the coastal area(Fig.11a). In SEA(Fig.11c), land in the PRD is replaced by ocean. The barrier effects of the coastline and mountains are missing, and the water vapor mixing ratio in the PRD is lower than that in HGT0

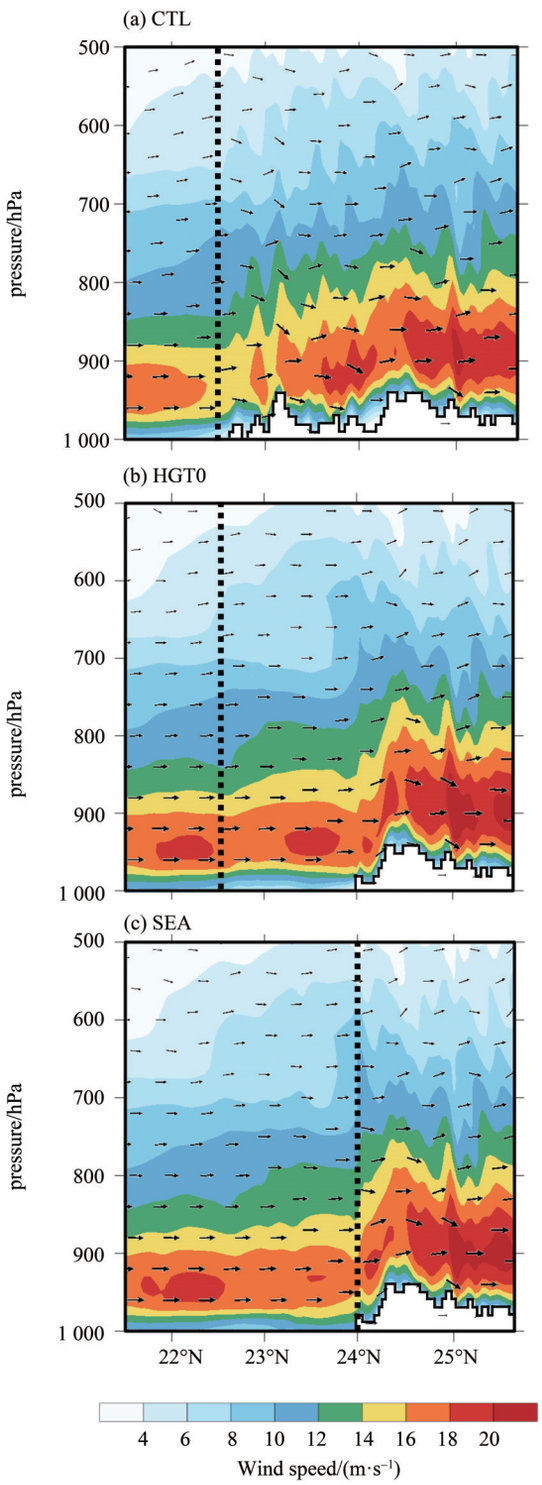

The black dash lines indicate the coastline.

Fig. 9　Vertical profile of wind speed (shading) and flow vectors (black vector; the vertical velocity has been magnified tenfold) along the black line (from point A to point B along 114. 8°E) in Fig.2b for the (a) CTL, (b) HGT0 and (c) SEA runs at 2000 UTC 10 May 2014

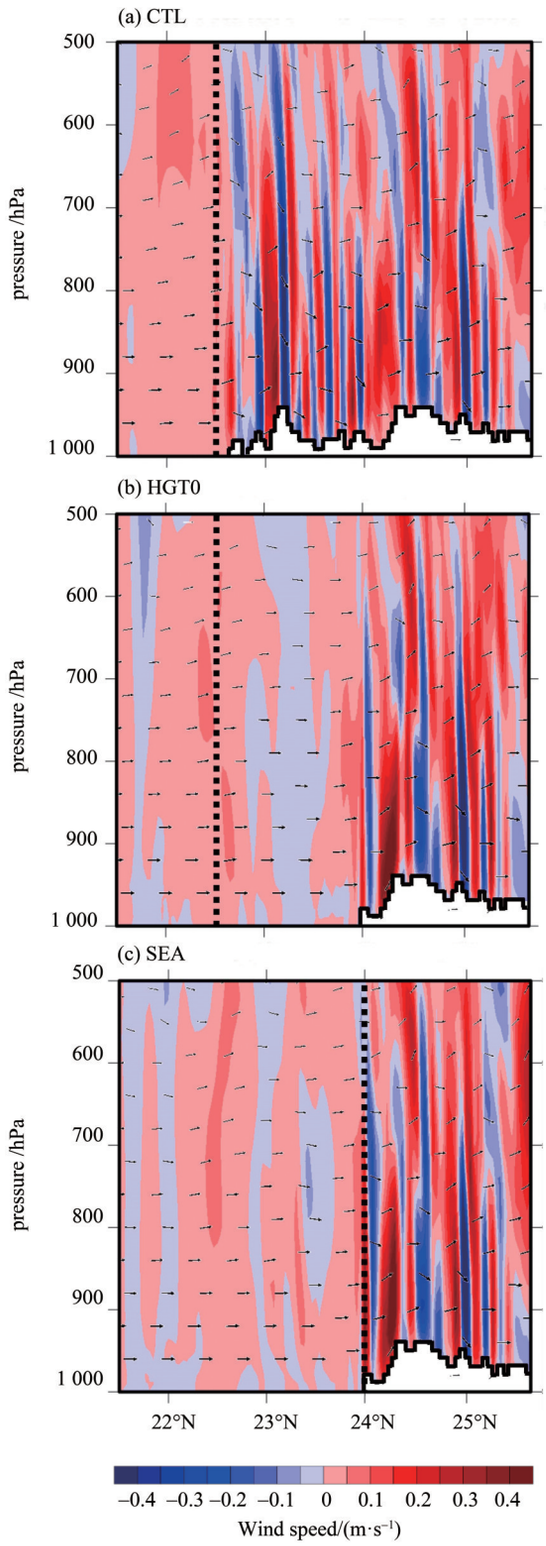

The black dash lines indicate the coastline.

Fig. 10　Vertical profile of vertical velocity (shading) and wind field flow vectors (black vector; the vertical velocity has been magnified tenfold) along the black line (from point A to point B along 114. 8°E) in Fig.2b for the (a) CTL, (b) HGT0 and (c) SEA runs at 2000 UTC 10 May 2014

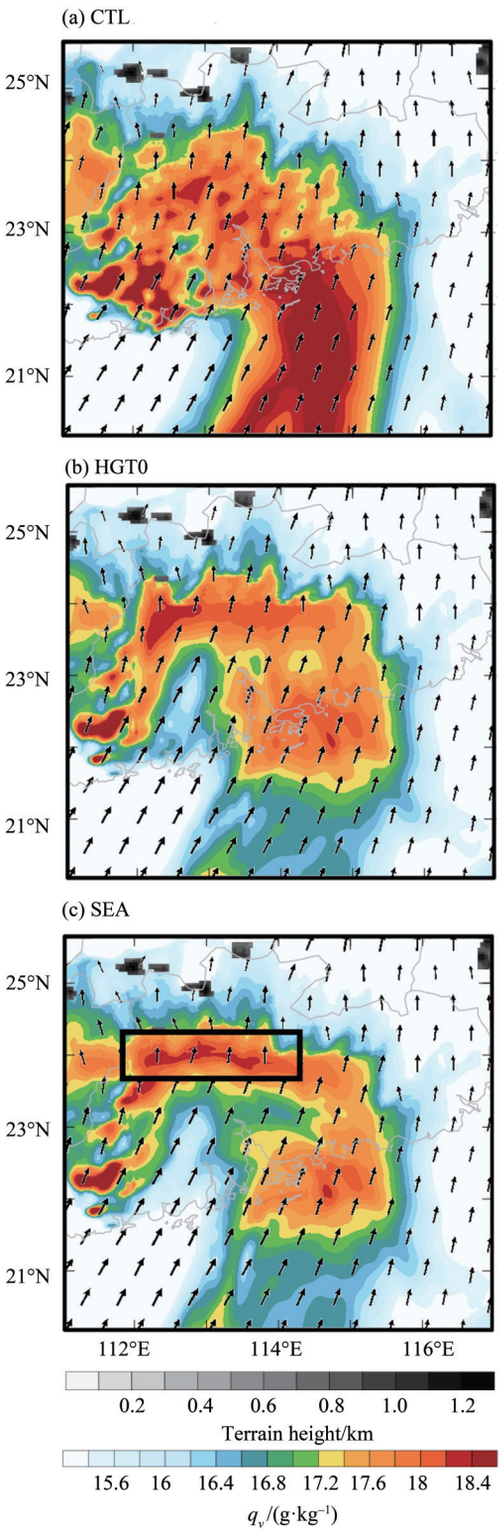

In (c), black box indicates the new coastline.

Fig. 11 Terrain height (gray-scale shading) overlaid with water vapor mixing ratio(color shading) and horizontal wind velocity at 925 hPa (vectors) in domain D03(see Fig.1) for the (a) CTL, (b) HGT0 and (c) SEA runs at 2000 UTC 10 May 2014

(Fig.11c). In the absence of orographic lifting and the contrast of frictional forces between sea and land, there is no convergence of water vapor. Therefore, there is little accumulation of water vapor in the PRD in SEA. On the contrary, water vapor mixing ratio is high along the new coastline, with maximum value exceeding 18. 4 g/kg. This is because water vapor is blocked by the new coastline and mountain topography, and the moisture accumulates on the windward slopes of the mountains along the new coastline(black box; Fig.11c).

We conducted a quantitative examination of the interaction between terrain and water vapor transport. Fig.12 shows the evolution of the average water vapor mixing ratio in the PRD in the three experiments over the 13 hours(1200 UTC 10 May-0100 UTC 11 May) between the beginning of the simulation and the start of precipitation. In CTL, HGT0 and SEA, the average water vapor mixing ratio increases between 1200 and 2200 UTC on 10 May. Because of the barrier effects of the coastline and mountains, average water vapor mixing ratio is the highest in CTL and peaks at 18. 2 g/kg. The average water vapor mixing ratio in HGT0 is relatively low and peaks at only approximately 17. 6 g/kg. Because of the absence of coastlines and mountains in the PRD, average water vapor mixing ratio is the lowest in SEA and peaks at only around 17. 3 g/kg. Between 2200 UTC 10 May and 0100 UTC 11 May, the water vapor content at 925 hPa begins to decrease, and continues to decline because of precipitation. Our results show that the coastline and the low mountains in the PRD can effectively block the diffusion of moisture and lock the water vapor in coastal areas and around windward slopes, accumulating sufficient moisture for precipitation.

5 Conclusions

In this study, we used the WRF-Chem model to conduct a series of sensitivity experiments of a typical case of warm-sector heavy rainfall(11 May 2014) in South China, and analyzed the impact of the coastline and terrain in the PRD region on the precipitation process in terms of dynamics and water vapor transport.

We examined the influence of the coastline and

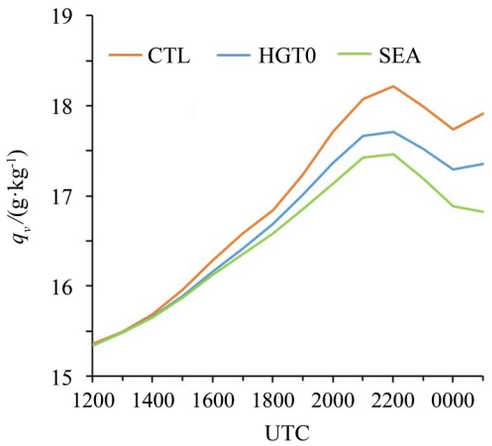

Fig. 12　Evolution of water vapor mixing ratio at 925 hPa averaged over the red box in Fig. 2 for the CTL, HGT0 and SEA runs from 1200 UTC 10 May to 0100 UTC 11 May

low mountain topography on warm-sector heavy rainfall distribution and intensity. Compared with results from CTL, precipitation in HGT0 starts 6 h later, is mainly confined to the north of 22. 7°N which is 80 km north than in CTL in 12 hours accumulation, and is weaker, because terrain height in the PRD is set to 0 m. Compared with results from CTL, precipitation in SEA starts 8 h later, is almost vanished in the PRD, and has a precipitation center on the new coastline, because the land in the PRD is replaced by ocean. Furthermore, in the PRD, there are no clear regions with heavy precipitation; high precipitation rates are mostly concentrated along the new coastline, and area with high precipitation rates is only half that in CTL.

In terms of dynamic effects, the wide mountain range consisting of low mountains plays a role in orographic uplifting and triggers convection generation. Additionally, convergence occurs along the coastline because of the contrast of frictional forces between land and ocean. These two factors greatly affect the generation and development of convection along the coastline and in the mountainous areas of the PRD, thereby influencing the intensity and distribution of precipitation.

In terms of water vapor transport, the coastline and mountains can effectively block and collect the low-level humid airflow from the sea, so that moisture can accumulate along the coast and on the windward slopes of mountains. In the sensitivity experiment where terrain height is set to 0 m, the water vapor content increases along the coast; water vapor is transported across the entire study area as a result of convergence caused by land surface friction; the maximum average water vapor mixing ratio in this experiment is lower than that in the control experiment by 0. 8g/kg. In the sensitivity experiment where the land in the PRD is replaced by ocean, the water vapor content in the PRD is greatly reduced in the absence of orographic lifting and the contrast of frictional forces between sea and land; water vapor accumulates along the new coastline in the northern part of the PRD; the maximum average water vapor mixing ratio in this sensitivity experiment is lower than that in the control experiment by 1. 1 g/kg. This indicates that the coastline and terrain can effectively lock moisture and accumulate sufficient water vapor for precipitation to occur.

We conclude that the coastline and mountain topography in the PRD region affect the distribution and intensity of the warm-sector heavy rainfall. In the experiment where the mountain topography is removed, the 12 hours accumulated precipitation area is mainly confined to the north of 22. 7°N which is 80 km north than without moving out the mountains, and precipitation intensity decreases. In the experiment where the coastline is moved to the northern part of the PRD, the precipitation area almost disappeared in the PRD, and has a precipitation center on the new coastline; the area with high precipitation rates is only half that in the control experiment. Therefore, coastline and mountain topography in the PRD has substantial influence on the occurrence, intensity and distribution of warm-sector torrential rainfall. Our findings will be useful for future precipitation forecasts and disaster prevention in the PRD region.

References:

[1] HUANG S S, LI Z G, BAO C L, et al. Rainstorms during pre-rainy season in South China [M]. Guangzhou: Guangdong Science and Technology Press, 1986.

[2] TAO S Y. Rainstorms in China [M]. Beijing: Science

Press, 1980.

[3] LIN L X, FENG Y R, HUANG Z, et al. Technical guidance on weather forecasting in Guangdong Province [M]. Beijing: China Meteorological Press, 2006.

[4] WU N, WEN Z, DENG W, et al. Advances in warm-sector heavy rainfall during the first rainy season in South China [J]. Journal of the Meteorological Sciences, 2020, 40(5): 605−616.

[5] GROSSMAN R L, DURRAN D R. Interaction of low-level flow with the western ghat mountains and offshore convection in the summer monsoon[J]. Monthly Weather Review, 1984, 112(4): 652−672.

[6] HOUZE R A, WILTON D C, SMULL B F. Monsoon convection in the Himalayan region as seen by the TRMM Precipitation Radar [J]. Quarterly Journal of the Royal Meteorological Society, 2007, 133(627): 1389−1411.

[7] XIE S P, XU H, SAJI N H, et al. Role of narrow mountains in large-scale organization of Asian monsoon convection [J]. Journal of Climate, 2006, 19(14): 3420−3429.

[8] DING Y H, CHAN J C L. The East Asian summer monsoon: An overview [J]. Meteorology and Atmospheric Physics, 2005, 89(1): 117−142.

[9] BAI L, CHEN G, HUANG L. Convection initiation in monsoon coastal areas (South China) [J]. Geophysical Research Letters, 2020, 47(11): e2020GL087035. DOI: 10. 1029/2020GL087035.

[10] DU Y, CHEN G, HAN B, et al. Convection initiation and growth at the coast of South China. Part II: Effects of the terrain, coastline, and cold pools [J]. Monthly Weather Review, 2020, 148(9): 3871−3892.

[11] BUZZI A, TARTAGLIONE N, MALGUZZI P. Numerical simulations of the 1994 Piedmont Flood: role of orography and moist processes[J]. Monthly Weather Review, 1998, 126(9): 2369−2383.

[12] BERGERON T. The problem of artificial control of rainfall on the globe: II. The coastal orographic maxima of precipitation in autumn and winter [J]. Tellus, 1949, 1(3): 15−32.

[13] LEE J T, LEE D I, SHIMIZU S, et al. Analysis of determinants for an enhanced and long-lasting coastal convective system by means of a case study (26 July 2011) [J]. Advances in Atmospheric Sciences, 2019, 36(12): 1327−1339.

[14] LEE J T, LEE D I, YOU C H, et al. Dual-Doppler radar analysis of a near-shore line-shaped convective system on 27 July 2011, Korea: a case study [J]. Tellus A: Dynamic Meteorology and Oceanography, 2014, 66(1): 23453.

[15] LIN Y L, CHIAO S, WANG T A, et al. Some common ingredients for heavy orographic rainfall [J]. Weather and Forecasting, 2001, 16(6): 633−660.

[16] YU C K, JORGENSEN D P, ROUX F. Multiple precipitation mechanisms over mountains observed by airborne Doppler radar during MAP IOP5 [J]. Monthly Weather Review, 2007, 135(3): 955−984.

[17] BUZZI A, FOSCHINI L. Mesoscale meteorological features associated with heavy precipitation in the southern Alpine region [J]. Meteorology and Atmospheric Physics, 2000, 72(2): 131−146.

[18] NUISSIER O, DUCROCQ V, RICARD D, et al. A numerical study of three catastrophic precipitating events over southern France. I: Numerical framework and synoptic ingredients [J]. Quarterly Journal of the Royal Meteorological Society, 2008, 134(630): 111−130.

[19] TU C C, CHEN Y L, LIN P L, et al. Characteristics of the marine boundary layer jet over the south china sea during the early summer rainy season of Taiwan [J]. Monthly Weather Review, 2019, 147(2): 457−475.

[20] MIGLIETTA M M, ROTUNNO R. Numerical simulations of conditionally unstable flows over a mountain ridge [J]. Journal of the Atmospheric Sciences, 2009, 66(7): 1865−1885.

[21] MIGLIETTA M M, ROTUNNO R. Numerical simulations of Low-CAPE flows over a mountain ridge [J]. Journal of the Atmospheric Sciences, 2010, 67(7): 2391−2401.

[22] MIGLIETTA M M, ROTUNNO R. Application of theory to simulations of observed cases of orographically forced convective rainfall [J]. Monthly Weather Review, 2012, 140(9): 3039−3053.

[23] MIGLIETTA M M, ROTUNNO R. Numerical simulations of sheared conditionally unstable flows over a mountain ridge [J]. Journal of the Atmospheric Sciences, 2014, 71(5): 1747−1762.

[24] CHEN G T J, YU C C. Study of low-level jet and extremely heavy rainfall over northern Taiwan in the Mei-Yu season [J]. Monthly Weather Review, 1988, 116(4): 884−891.

[25] DAVIS C A, LEE W C. Mesoscale analysis of heavy rainfall episodes from SoWMEX/TiMREX [J]. Journal of the Atmospheric Sciences, 2012, 69(2): 521−537.

[26] KUO Y C, LEE M A, LU M M. Association of Taiwan's rainfall patterns with large-scale oceanic and atmospheric phenomena [J]. Advances in Meteorology, 2016, 2016: 3102895.

[27] LI J, CHEN Y L, LEE W C. Analysis of a heavy rainfall event during TAMEX [J]. Monthly Weather Review, 1997, 125(6): 1060−1082.

[28] XU W, ZIPSER E J, CHEN Y L, et al. An orography-associated extreme rainfall event during TiMREX: Initiation, storm evolution, and maintenance [J]. Monthly Weather Review, 2012, 140(8): 2555−2574.

[29] DU Y, CHEN G. Climatology of low-level jets and their impact on rainfall over Southern China during the

early-summer rainy season [J]. Journal of Climate, 2019, 32(24): 8813−8833.

[30] FU P, ZHU K, ZHAO K, et al. Role of the nocturnal low-level jet in the formation of the morning precipitation peak over the Dabie Mountains [J]. Advances in Atmospheric Sciences, 2019, 36(1): 15−28.

[31] ZHAO Y. Numerical investigation of a localized extremely heavy rainfall event in complex topographic area during midsummer[J]. Atmospheric Research, 2012, 113: 22−39.

[32] CHEN X, ZHANG F, ZHAO K. Influence of monsoonal wind speed and moisture content on intensity and diurnal variations of the Mei-Yu Season coastal rainfall over South China [J]. Journal of the Atmospheric Sciences, 2017, 74(9): 2835−2856.

[33] DU Y, CHEN G. Heavy rainfall associated with double low-level jets over Southern China. Part II: Convection Initiation [J]. Monthly Weather Review, 2019, 147(2): 543−565.

[34] LI H, WAN Q, PENG D, et al. Multiscale analysis of a record-breaking heavy rainfall event in Guangdong, China [J]. Atmospheric Research, 2020, 232: 104703. DOI:10. 1016/j. atmosres. 2019. 104703.

[35] LUO Y, SUN J, LI Y, et al. Science and prediction of heavy rainfall over China: Research progress since the reform and opening-up of new China [J]. Journal of Meteorological Research, 2020, 34(3): 427−459.

[36] LUO Y, ZHANG R, WAN Q, et al. The southern China monsoon rainfall experiment (SCMREX) [J]. Bulletin of the American Meteorological Society, 2017, 98(5): 999−1013.

[37] WU N, ZHUANG X, MIN J, et al. Practical and intrinsic predictability of a warm-sector torrential rainfall event in the South China monsoon region[J]. Journal of Geophysical Research: Atmospheres, 2020, 125(4): e2019JD031313.

[38] JOYCE R J, JANOWIAK J E, ARKIN P A, et al. CMORPH: A method that produces global precipitation estimates from passive microwave and infrared data at high spatial and temporal resolution [J]. Journal of Hydrometeorology, 2004, 5(3): 487−503.

[39] HOU T, KONG F, CHEN X, et al. Impact of 3DVAR data assimilation on the prediction of heavy rainfall over Southern China [J]. Advances in Meteorology, 2013,2013: 129642. DOI:10. 1155/2013/129642.

[40] GRELL G A, DÉVÉNYI D. A generalized approach to parameterizing convection combining ensemble and data assimilation techniques[J]. Geophysical Research Letters, 2002, 29(14):1693. DOI:10. 1029/2002GL015311.

[41] LIN Y L, FARLEY R D, ORVILLE H D. Bulk parameterization of the snow field in a cloud model [J]. Journal of Climate and Applied Meteorology, 1983, 22(6): 1065−1092.

[42] HONG S Y, NOH Y, DUDHIA J. A new vertical diffusion package with an explicit treatment of entrainment processes [J]. Monthly Weather Review, 2006, 134(9): 2318−2341.

[43] IACONO M J, DELAMERE J S, MLAWER E J, et al. Radiative forcing by long-lived greenhouse gases: Calculations with the AER radiative transfer models [J]. Journal of Geophysical Research: Atmospheres, 2008, 113(D13): D13103. http://doi. org/10. 1029/2008JD009944.

[44] LIVNEH B, RESTREPO P J, LEITENMAIER D P. Development of a unified land model for prediction of surface hydrology and land-atmosphere interactions [J]. Journal of Hydrometeorology, 2011, 12(6): 1299−1320.

[45] JIMENEZ P A, DUDHIA J, GONZALEZ-ROUCO J F, et al. A revised scheme for the WRF surface layer formulation [J]. Monthly Weather Review, 2012, 140(3): 898−918.

[46] ZAVERI R A, PETERS L K. A new lumped structure photochemical mechanism for large-scale applications [J]. Journal of Geophysical Research: Atmospheres, 1999, 104(D23): 30387−30415.

[47] ZAVERI R A, EASTER R C, FAST J D, et al. Model for simulating aerosol interactions and chemistry(MOSAIC) [J]. Journal of Geophysical Research-Atmospheres, 2008, 113(D13): D13204. https://doi. org/10. 1029/2007JD008782.

[48] BARNARD J C, CHAPMAN E G, FAST J D, et al. An evaluation of the FAST-J photolysis algorithm for predicting nitrogen dioxide photolysis rates under clear and cloudy sky conditions [J]. Atmospheric Environment, 2004, 38(21): 3393−3403.

[49] WILD O, ZHU X, PRATHER M J. Fast-j: Accurate simulation of in- and below-cloud photolysis in tropospheric chemical models [J]. Journal of Atmospheric Chemistry, 2000, 37(3): 245−282.

[50] LI M, ZHANG Q, STREETS D G, et al. Mapping Asian anthropogenic emissions of non-methane volatile organic compounds to multiple chemical mechanisms [J]. Atmospheric Chemistry and Physics, 2014, 14(11): 5617−5638.

[51] GUENTHER A, KARL T, HARLEY P, et al. Estimates of global terrestrial isoprene emissions using MEGAN (Model of Emissions of Gases and Aerosols from Nature) [J]. Atmospheric Chemistry and Physics, 2006, 6 (11): 3181−3120.

（责任编辑　秦社彩）